








Structural transition and anisotropic magnetism in disordered Zintl phase  $\text{Eu}_7\text{Ga}_6\text{Sb}_8$ 

Matthew S. Cook , Elizabeth A. Peterson , Clément Girod, Ashley Weiland , Jian-Xin Zhu ,  
J. D. Thompson, Sean M. Thomas , and Priscila F. S. Rosa   
*Los Alamos National Laboratory, Los Alamos, New Mexico 87545, USA*

 (Received 4 April 2023; revised 14 August 2023; accepted 30 August 2023; published 15 September 2023)

Single crystals of the Zintl compound  $\text{Eu}_7\text{Ga}_6\text{Sb}_8$  were synthesized using a Ga-Sb flux. We report the temperature ( $T$ ) and magnetic field ( $H$ ) dependence of the magnetic susceptibility ( $\chi$ ), magnetization ( $M$ ), resistivity ( $\rho$ ), specific heat ( $C$ ), and thermal expansion ( $\alpha$ ). We also report high-resolution powder x-ray diffraction data that support a structural phase transition with accompanying signatures seen in  $C(T)$ ,  $\rho(T)$ , and  $\alpha(T)$ . We find  $\text{Eu}_7\text{Ga}_6\text{Sb}_8$  exhibits antiferromagnetic ordering at  $T_{N1} = 9.0$  K from anomalies seen in  $\chi(T)$ ,  $C(T)$ , and  $\alpha(T)$ , as well as a potential reorientation of  $\text{Eu}^{2+}$  spins at  $T_{N2} = 7.5$  K and  $T_{N3} = 7.2$  K. Density functional theory calculations predict  $\text{Eu}_7\text{Ga}_6\text{Sb}_8$  to be semiconducting; however, electrical resistivity measurements show bad-metal behavior that indicates the presence of disorder.

DOI: [10.1103/PhysRevMaterials.7.094601](https://doi.org/10.1103/PhysRevMaterials.7.094601)

## I. INTRODUCTION

Zintl phases represent a large group of intermetallic compounds that are generally composed of electropositive alkali or alkaline-earth metals and electronegative post-transition metals or metalloids (groups 13–16). A wide range of ternary Zintl phases can also be formed with rare-earth elements paired with group 12–14 elements as well as group 15 elements that have greater electronegativity [1–3]. A Zintl phase consists of an electropositive network of cations that donate electrons to the covalently bonded electronegative polyanions. There is a complete electron transfer in order to fill the valence states of the polyanions, thus satisfying the octet rule. As a result, semiconducting behavior is expected in an electron-precise Zintl compound [4].

Although the Zintl concept has proven to be a useful interpretation of the bonding within particular compositions of intermetallic materials, there are many examples of compounds that are thought to follow the electron counting rules, yet show metallic behavior [5–7]. This is commonly found when there is a weak polarity of the covalent bonding, i.e., a small difference in electronegativity between the polyanions and cations. Thus, new properties within a diverse range of Zintl compositions can be discovered through substitutions that affect the electronegativity difference of the framework.

When one considers the different properties of constituent atoms, such as valence electron configuration and atomic radii, different structural motifs become energetically favorable [8]. A wide range of structures has been found to adhere to the Zintl rule, wherein the anionic framework can have a dimensionality of zero (molecular), one, two, or three [9]. Many of these structures are unstable to pressure, temperature, and chemical doping. Structural phase transitions therefore have been theorized and observed in several Zintl families [10–13]. Low-dimensional layered structures in particular are prone to structural phase transitions, with the most notable examples being layered chalcogenides [14–18]. There is generally a competition of covalent and ionic bonding in these

materials, and different bonding configurations that are very close in energy produce structural polymorphs. Layered Zintl phases naturally fall into this reasoning; the competition of ionic and covalent bonding is deterministic of the electronic and structural properties.

Over the past two decades, Zintl phases have attracted much interest for their thermoelectric properties, as their particular structures and bonding result in phonon-glass electron-crystal properties that give them a high thermoelectric figure of merit. The cations in the Zintl framework scatter heat-transferring phonons to give these materials low lattice thermal conductivity, while the anions serve as the electron crystal in providing a high-mobility semiconducting electronic structure [19]. Other more recent applications of these materials include optoelectronics, photovoltaics, catalysis, and dark matter detection [20–25]. From a fundamental standpoint Zintl phases have been found to host many exotic states of matter, such as topological phases, superconductivity, and anomalous Hall effect [26–32]. Additionally, rare-earth cations within Zintl compounds generally display magnetic ordering and offer a platform for emergent phenomena such as colossal magnetoresistance and complex magnetic structures [25,33–36].

The synthesis and characterization of  $\text{Eu}_7\text{Ga}_6\text{Sb}_8$  was first reported in Ref. [1] wherein small crystals were obtained from a solid-state reaction. Park *et al.* determined the crystal structure at 173 K and found that this compound crystallizes in the orthorhombic space group  $Pbca$  (No. 61). They also determined the band gap of  $\text{Eu}_7\text{Ga}_6\text{Sb}_8$  to be 0.6 eV from infrared spectroscopy, which is consistent with their electronic structure calculations. Lastly antiferromagnetic ordering at 9 K was detected, in agreement with the divalent nature of Eu ions in  $\text{Eu}_7\text{Ga}_6\text{Sb}_8$ .

In this work we have synthesized single crystals of  $\text{Eu}_7\text{Ga}_6\text{Sb}_8$  using the flux technique. We find evidence of a structural transition near  $T = 250$  K with powder x-ray diffraction (PXRD), resistivity, specific heat, and thermal expansion measurements. Antiferromagnetic ordering with

transition temperature  $T_{N1} = 8.9$  K is observed in magnetization, resistivity, specific heat, and dilatometry measurements. The anisotropy observed in  $\chi(T)$  and  $M(H)$  suggests a complex magnetic structure. There is a metamagnetic transition revealed in the magnetization vs field measurements when the field is applied in plane at approximately 1 T. Based on our thermodynamic and electrical transport data, we build a magnetic phase diagram that is consistent across these experiments. The entropy associated with antiferromagnetic order only reaches 80% of that expected for a divalent Eu ion with  $S = 7/2$ , suggesting that magnetic frustration may be present. Electrical resistivity measurements show weak metallic behavior at high temperatures followed by a nonactivated increase on cooling. Though density functional theory predicts this material to have a semiconducting ground state, disorder likely plays a large role in electrical transport.

## II. EXPERIMENTAL METHODS

Single crystals of  $\text{Eu}_7\text{Ga}_6\text{Sb}_8$  were grown in a self-flux with a molar ratio of  $7:112:14 = \text{Eu}:\text{Ga}:\text{Sb}$ . These elements were placed into an alumina crucible and then enclosed in a quartz ampoule that was first flushed with argon gas and then flame sealed under vacuum. The ampoule was then heated to  $1050^\circ\text{C}$  and slowly cooled at  $2^\circ\text{C}/\text{h}$  to  $350^\circ\text{C}$  and subsequently heated back to  $500^\circ\text{C}$  to decant the single crystals from the molten flux. This growth method produces dark gray hexagonal plates of up to 3 mm.

Phase purity at room temperature was confirmed through powder x-ray diffraction using  $\text{CuK}\alpha$  radiation with a Malvern PANalytical Empyrean x-ray diffractometer. Rietveld refinement was performed using the Highscore software suite [37]. High-resolution synchrotron powder x-ray diffraction data ( $\lambda = 0.457861 \text{ \AA}$ ) were collected to  $2\theta = 28^\circ$  at the 11-BM beamline at the Advanced Photon Source of Argonne National Laboratory. Discrete detectors collected data points every  $0.001^\circ$  with a scan speed of  $0.01 \text{ s}^{-1}$  at room temperature. Pawley refinements were carried out with the TOPAS-Academic software. The elemental stoichiometry of the samples was confirmed through energy-dispersive x-ray spectroscopy (EDX). Our result,  $\text{Eu}_{7.0(2)}\text{Ga}_{5.7(2)}\text{Sb}_{8.2(3)}$ , agrees well with the previously reported stoichiometry  $\text{Eu}_{7.0(2)}\text{Ga}_{5.8(2)}\text{Sb}_{8.3(2)}$  [1].

Magnetic measurements were performed in a commercial MPMS SQUID magnetometer with fields up to 6.5 T. Standard four-point electrical resistivity measurements were performed in a commercial PPMS helium-4 cryostat using a Lake Shore Cryotronics Model 372 AC resistance bridge.  $25 \mu\text{m}$  platinum wires used attached to gold sputtered pads with silver paint on clean crystal surfaces. Specific heat measurements were performed in a commercial PPMS system using a thermal relaxation technique. Thermal expansion and magnetostriction data were taken with a capacitive dilatometer as described in Ref. [38].

First-principles calculations were performed using density functional theory (DFT) with a plane-wave basis and projector augmented wave pseudopotentials [39] as implemented in the Vienna *ab initio* simulation package (VASP) [40,41]. Electronic structure calculations were performed in the generalized-gradient approximation (GGA) as

implemented by Perdew, Burke, and Ernzerhof [42]. A 500 eV energy cutoff was used with a  $5 \times 5 \times 5$   $\Gamma$ -centered  $k$ -point grid. Structures were relaxed until forces were less than  $1 \text{ meV}/\text{\AA}$ . Band structures were calculated with the Eu  $f$  electrons confined to the core as well as treated explicitly with a Hubbard- $U$  correction ( $U = 6.0 \text{ eV}$ ) as implemented by Dudarev *et al.* [43].

## III. RESULTS

### A. Structure

The crystal structure of  $\text{Eu}_7\text{Ga}_6\text{Sb}_8$  was previously determined at 173 K [1]. Rietveld refinements of our low-temperature (180 K), high-resolution powder x-ray diffraction confirm that  $\text{Eu}_7\text{Ga}_6\text{Sb}_8$  crystallizes in the  $Pbca$  orthorhombic space group (61) with lattice parameters of  $a = 15.645 \text{ \AA}$ ,  $b = 17.289 \text{ \AA}$ , and  $c = 17.916 \text{ \AA}$ . Previous work suggested the room-temperature structure to be orthorhombic within space group  $Cmcm$  (63). Thermodynamic evidence supports a structural phase transition at  $T = 250 \text{ K}$  and will be further discussed in the following sections. Pawley refinements of room-temperature high-resolution powder x-ray diffraction corroborate this claim. The extracted lattice parameters are  $a = 8.997 \text{ \AA}$ ,  $b = 15.618 \text{ \AA}$ , and  $c = 17.319 \text{ \AA}$  [44]. Figure 1 shows the refinements of both room-temperature and low-temperature data sets. Figure 1(a) shows the room-temperature data overlaid with a Pawley fit of the  $Cmcm$  structure, and Fig. 1(b) shows the Rietveld refinement of the 180 K data with the  $Pbca$  structure. Figures 1(c) and 1(d) show zoomed regions of the 300 K (c) and 180 K (d) data to highlight the differences in the  $Cmcm$  and  $Pbca$  fits for both data sets. We conclude that  $Cmcm$  is best suited to model the high-temperature data and  $Pbca$  is a better fit to the low-temperature data.

### B. Magnetization

The crystal structure of  $\text{Eu}_7\text{Ga}_6\text{Sb}_8$  contains 7 unique  $\text{Eu}^{2+}$  sites that result in complex and anisotropic magnetic ordering at low temperatures. The temperature dependence of the magnetic susceptibility given by  $\chi = M/H$  is shown in Fig. 2(a).

A magnetic field of  $\mu_0 H = 0.1 \text{ T}$  was applied parallel ( $\chi_c$ ) and perpendicular ( $\chi_{ab}$ ) to the  $c$  axis of the crystal. A fit of inverse susceptibility to the Curie-Weiss model gives an effective moment of  $\mu_{\text{eff}} = 7.88(1) \mu_B/\text{Eu}$  and  $\mu_{\text{eff}} = 8.14(1) \mu_B/\text{Eu}$  for  $\chi_{ab}$  and  $\chi_c$ , respectively. These values are consistent with the Hund's rule moment of a bare  $\text{Eu}^{2+}$  ion. The slightly positive Curie-Weiss temperatures of  $\theta_c = 0.16(8) \text{ K}$  and  $\theta_{ab} = 0.4(1) \text{ K}$  are indicative of ferromagnetic (FM) exchange interactions at high temperatures, which is in contrast with the low-temperature antiferromagnetic (AFM) transitions seen in the magnetic susceptibility. There are many examples of divalent europium compounds that have a positive Curie-Weiss temperature while also showing antiferromagnetic ordering at low temperatures [25,33,45–50]. This has generally been attributed to competing magnetic exchange interactions.

With  $H \perp c$  there are three clear transitions in the  $\chi_{ab}(T)$  plot shown in the inset of Fig. 2(a) at  $T_{N1} = 9.0 \text{ K}$ ,  $T_{N2} = 7.5 \text{ K}$ , and  $T_{N3} = 7.2 \text{ K}$ , determined by the intercepts in the

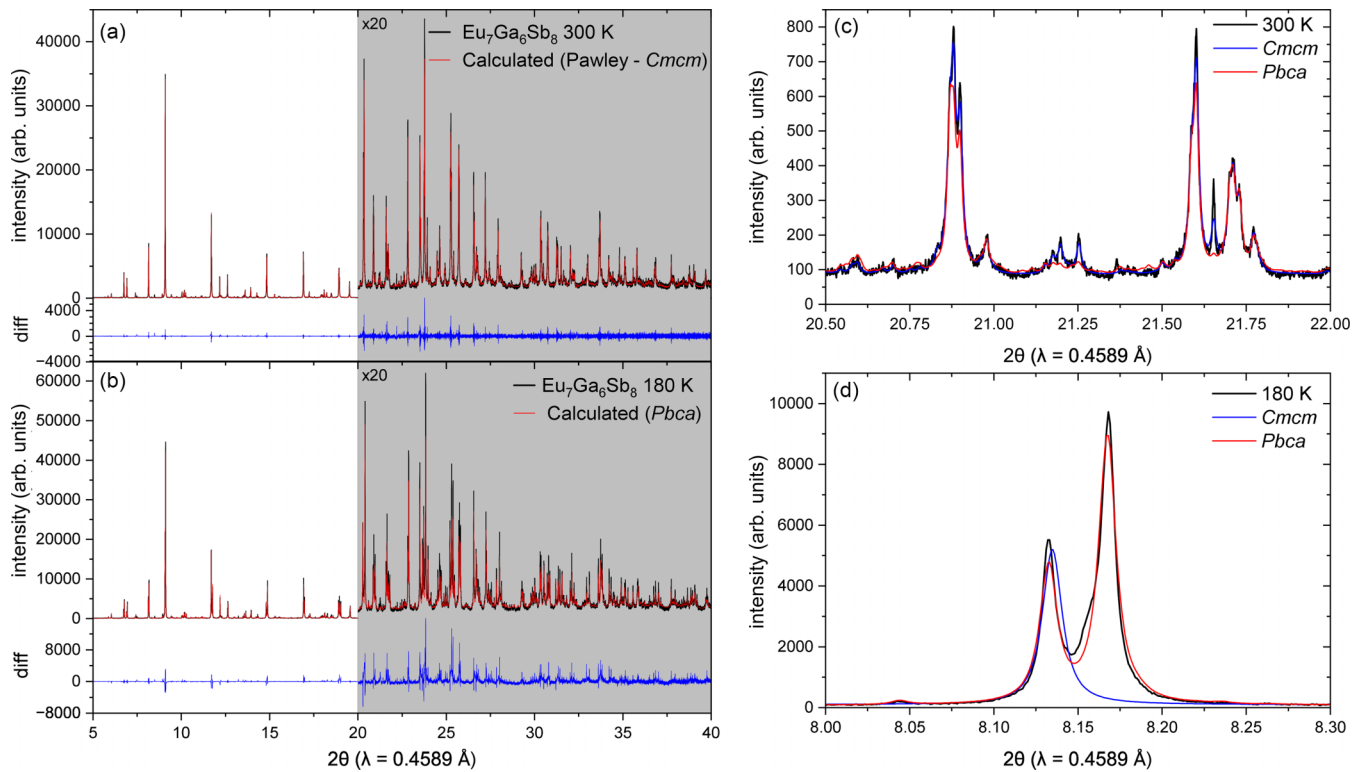


FIG. 1. Panels (a) and (b) show observed (black), calculated (red), and difference (blue, bottom) synchrotron powder x-ray diffraction patterns for  $\text{Eu}_7\text{Ga}_6\text{Sb}_8$  at both 300 K and 180 K. Panel (a) shows the room-temperature data overlain with the calculated  $Cmcm$  structure. Panel (b) shows the data at 180 K with the  $Pbca$  structure overlain. The difference pattern is plotted at the same scale as the other data. Panels (c) and (d) compare  $Cmcm$  and  $Pbca$  for both 300 K (c) and 180 K (d) data sets highlighting regions indicating why  $Cmcm$  is a better model for the room-temperature data and  $Pbca$  is a better model for the low-temperature data. The collected data are shown in black, the  $Cmcm$  fit is in blue, and the  $Pbca$  fit is in red.

jumps of  $d\chi/dT$ . These transitions correspond to peaks observed in the specific heat. The lower two transitions,  $T_{N2}$  and  $T_{N3}$ , are likely due to spin reorientation of the Eu moments, as was suggested for several divalent Eu compounds [47,51,52]. When  $H \parallel c$  there is only one obvious cusp in the magnetic susceptibility. Upon closer inspection, two similar features that correspond to  $T_{N2}$  and  $T_{N3}$  appear as a peak in the derivative of  $\chi_c(T)$  which is plotted in the inset of Fig. 2(b). These lower transitions have a very small effect on the susceptibility when  $H \parallel c$ , which may suggest that the spin reorientation happens in the  $ab$  plane; however, peaks in the specific heat for the same field direction confirm their existence.

The anisotropy of the magnetic susceptibility along both field directions is useful for inferring the possible spin structure of this compound. The magnitude of  $\chi_{ab}$  trends toward 0 as  $T \rightarrow 0$ , while  $\chi_c$  has a weak dependence on temperature with a slightly negative slope. This suggests that the AFM easy axis lies within the  $ab$  plane. The anisotropic low-temperature  $\chi(T)$  for different  $H$  is shown in Figs. 2(b) and 2(c). The transition  $T_{N1}$  is pushed to lower temperatures with increasing field in both directions; however, for  $H \perp c$  there is a slightly faster suppression. The lower transitions  $T_{N2}$  and  $T_{N3}$  become broad with increasing field and are suppressed by 2 T.

The isothermal  $M$  vs  $H$  plots in Figs. 2(e) and 2(f) provide supporting information of the possible magnetic structure of  $\text{Eu}_7\text{Ga}_6\text{Sb}_8$ .

When  $H \parallel c$ , the magnetization is linear in field at low fields and tends toward saturation at higher fields. No evidence of a field-induced transition is observed. These data, along with the anisotropy of the magnetic susceptibility shown in Fig. 2(a), suggest that the magnetic structure is likely coplanar, with the easy axis residing in the  $ab$  plane. A noncollinear structure cannot yet be ruled out with the information presented here.

In contrast to  $M(H)$  for  $H \parallel c$ -axis, Fig. 2(d) shows a field-induced transition for  $H \perp c$  at approximately  $H = 1.6$  T for  $T = 1.8$  K, which would again suggest that the AFM easy axis is parallel to the basal plane. This metamagnetic transition has a weak temperature dependence, and its critical field varies by less than 0.6 T as the temperature is lowered below  $T_{N1}$ . Metamagnetic transitions have been previously observed in several other antiferromagnetic Eu-based Zintl compounds [25,34,53].

### C. Resistivity

The temperature dependence of the electrical resistivity during cooling and heating is shown in Fig. 3(a). In the high-temperature region there is a sudden increase in the resistivity around 250 K. We attribute this anomaly to a structural transition based on powder x-ray diffraction data. There is also a noticeable effect in the resistivity above this transition with thermal cycling. The differences in resistivity after thermal

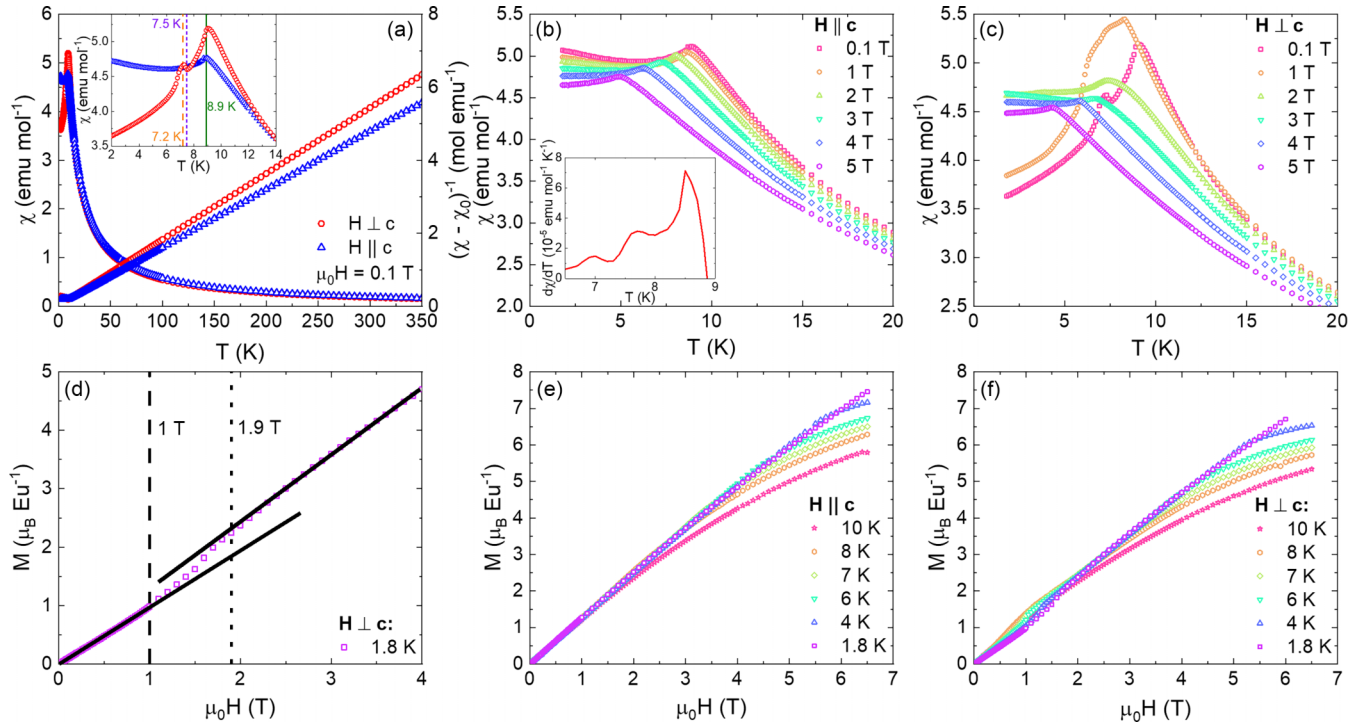


FIG. 2. (a) Left axis: Magnetic susceptibility versus temperature with the field aligned perpendicular and parallel to the  $c$  direction for  $\mu_0 H = 0.1$  T. Right axis: Inverse magnetic susceptibility versus temperature for  $\mu_0 H = 0.1$  T. For  $H \perp c$ ,  $\chi_0 = 0$ , but  $\chi_0$  is about 0.005% of the total  $\chi$  for  $H \parallel c$ . The small  $\chi_0$  in the latter case is due to a background signal from the sample-holder configuration. Inset: Low-temperature magnetic susceptibility versus field that shows two magnetic transitions, where  $T_{N1} = 9.0$  K and  $T_{N2} = 7.3$  K. (b), (c) Low-temperature magnetic susceptibility for  $H \parallel c$  and  $H \perp c$ , respectively, at various fields. Inset: Derivative of magnetic susceptibility  $\chi$  with respect to temperature  $T$  for  $H \parallel c$  showing two magnetic transitions. (d) Metamagnetic transition seen in the magnetization for  $H \perp c$  for  $T = 1.8$  K. (e), (f) Magnetization versus field for  $H \parallel c$  and  $H \perp c$ , respectively, at various temperatures near and below the magnetic transition.

cycling can be attributed to two parameters. First, there is hysteresis present from the structural change that is presumably a first-order phase transition. Second, as the sample is brought to liquid-helium temperatures and back, the resistivity values increase by about 25% between successive cycles. This is indicative of irreversible structural damage to the material.

In the low-temperature resistivity there is an anomaly associated with the antiferromagnetic ordering, as shown in the inset of Fig. 3(a). Slightly below  $T_{N1}$  there is a maximum in the resistivity which is preceded by a minimum in the proximity of  $T_{N2}$ .

In general, the resistivity has a weak temperature dependence with metallic behavior below the structural transition. At approximately 20 K the temperature dependence changes and there is an increase in the resistivity. An attempt to model this upturn by Kondo scattering behavior is shown in Fig. 3(b), where  $\rho \propto \ln(T)$ . The poor agreement (solid line) indicates that Kondo scattering is unlikely the cause of the low-temperature upturn. In addition, there are no obvious Kondo scattering centers in this purely divalent europium lattice. As DFT calculations predict this material to be an insulator, it is possible that this rise is due to the intrinsic band structure of  $\text{Eu}_7\text{Ga}_6\text{Sb}_8$ .

Intrinsic semiconductors should show activated behavior where the band gap can be estimated with an Arrhenius plot, as shown in Fig. 3(c). This plot does not contain any regions that are strictly linear, while the lowest temperature range shows a saturation behavior that is typical of semiconductors

with impurity bands. Conduction in disordered semiconductors has been previously modeled through Mott variable range hopping (VRH). In this model carriers hop between localized impurity states whose energy levels are close to the Fermi energy, which is assumed to be constant. The expression for  $n$ -dimensional VRH conduction is given by

$$\rho(T) = \rho_0 \exp\left(\frac{T_0}{T}\right)^{\frac{1}{n+1}}, \quad (1)$$

where  $T_0$  is the characteristic hopping temperature and  $\rho_0$  is the pre-exponential factor [54]. Efros and Shklovskii later found that long-range Coulomb correlations of localized electrons can lead to a gap in the density of states at the Fermi level [55]. In this case the conduction can also be described by Eq. (1) with  $n = 1$ . As shown in the inset of Fig. 3(b), attempts to fit the low-temperature resistivity to the various VRH models were unsuccessful.

One potential explanation for this temperature dependence is that the charge carriers responsible for weak metallic behavior are frozen out at low temperatures. For doped samples with low impurity concentrations, an impurity band can be well separated from the conduction band such that the carriers exhibit freeze-out at low enough temperatures [56]. This picture agrees with DFT if one considers that  $\text{Eu}_7\text{Ga}_6\text{Sb}_8$  likely exhibits self-doping from defect sites in this disordered structure.

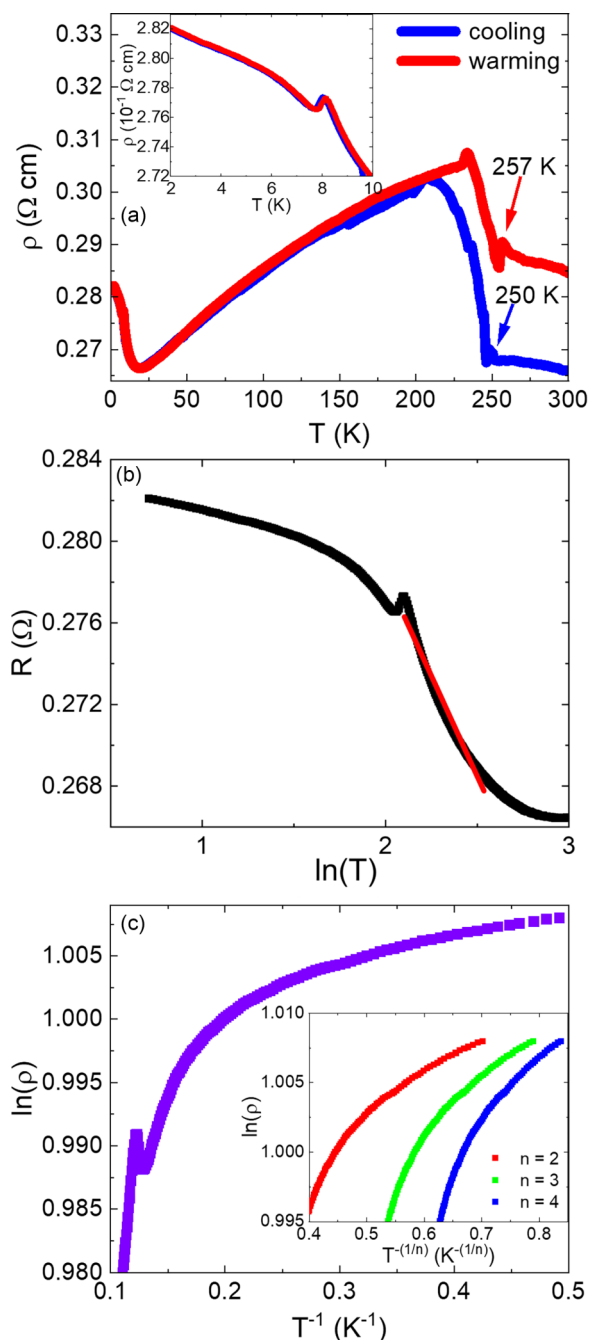


FIG. 3. (a) Resistivity versus temperature for the initial cool-down and subsequent warm-up of the sample. There is a large anomaly at  $T = 250$  K that signals a structural phase transition. Inset: Anomaly in the low-temperature resistivity due to magnetic ordering of  $\text{Eu}^{2+}$  moments. (b) Attempts at a linear fit of  $\rho$  vs  $\ln(T)$ , the temperature dependence expected for Kondo scattering. (c) Arrhenius plot of the low-temperature resistivity. Inset: Attempts at fitting the resistivity to the various types of variable range hopping conduction mechanisms, as described in the text.

An important caveat to this discussion of transport mechanisms is sample degradation as the temperature of the sample is cycled through the structural phase transition. These temperature cycles resulted in cracks forming throughout the single crystals, with the sample eventually breaking into

several pieces. This results in extrinsic scattering channels with varying temperature dependence. In-gap states as well as conduction across grain boundaries likely mask the intrinsic resistive behavior of this material.

#### D. Specific heat

Figure 4(a) shows the zero-field specific heat divided by temperature ( $C/T$ ) of  $\text{Eu}_7\text{Ga}_6\text{Sb}_8$  from 2 K to 300 K with the measured lattice contribution from the nonmagnetic analog  $\text{Ba}_7\text{Ga}_8\text{Sb}_8$  plotted as a solid red line. The inset of this figure shows an anomaly near 250 K that is attributed to a structural transition in the material.

Figure 4(b) shows  $C/T$  at multiple field values for  $2 \text{ K} \leq T \leq 15 \text{ K}$ . A sharp  $\lambda$ -like anomaly can be seen at the ordering temperature  $T_{N1} = 9.0 \text{ K}$ , consistent with the antiferromagnetic ordering inferred from magnetization measurements. There are also two smaller peaks that correspond to the spin-reorientation transitions in  $\chi(T)$  at  $T_{N2}$  and  $T_{N3}$ , which disappear when  $\mu_0 H \geq 2 \text{ T}$ . The sharp anomaly at  $T_N$  as well as the broad magnon-like feature below  $T_N$  are reminiscent of other  $\text{Eu}^{2+}$  antiferromagnetic compounds [25,35,50]. The specific heat due to spin excitations within AFM  $\text{Eu}^{2+}$  and  $\text{Gd}^{3+}$  ( $S = 7/2$ ) systems has been fitted using various exchange interactions as well as phenomenological spin wave models [57–59]. Precise modeling of the possible spin excitations within  $\text{Eu}_7\text{Ga}_6\text{Sb}_8$  is not yet feasible without more information on the magnetic structure of this compound.

In order to subtract a phonon contribution from the specific heat, we grew single crystals of a nonmagnetic analog with a closely related structure  $\text{Ba}_7\text{Ga}_8\text{Sb}_8$ . Though the structures are similar, they are not identical, and thus do not offer a perfect representation of the phonon contribution. The resulting subtraction  $C_{\text{mag}}/T$  was integrated to calculate the entropy associated with magnetic order in this compound. The results of this analysis are shown in Fig. 4(c). The entropy recovered at  $T_{N1} = 9.0 \text{ K}$  is only 80% of  $R \ln(8)$ , which suggests the presence of magnetic frustration. The magnetic entropy then saturates at approximately 90% of the expected value for a divalent Eu ion. The slight reduction from the expected entropy is likely due to the limitation of the phononic background.

#### E. Dilatometry

Thermal expansion measurements were performed to investigate the structural transition and to help map out the phase diagram. The relative change in length of the sample along the  $c$  axis  $\Delta L_c/L_c$  is presented in Fig. 5(a), where  $L$  is the length of the sample at room temperature. The thermal expansion was measured from  $2 \text{ K} < T < 300 \text{ K}$  while cooling and heating the sample. There are clear anomalies present near 250 K that agree with the anomalies found in resistivity and specific heat data, and point to a structural transition. The observed drops in  $\Delta L_c/L_c$  reflect a sudden contraction of the  $c$  axis due to the change in structure. As thermal cycling seems to have a measurable effect on the structural transition, these peaks also shift from the initial cool-down of the sample to the subsequent warming. Such behavior is also observed in the resistivity through thermal cycles and is indicative of a first-order phase transition as well as structural damage.

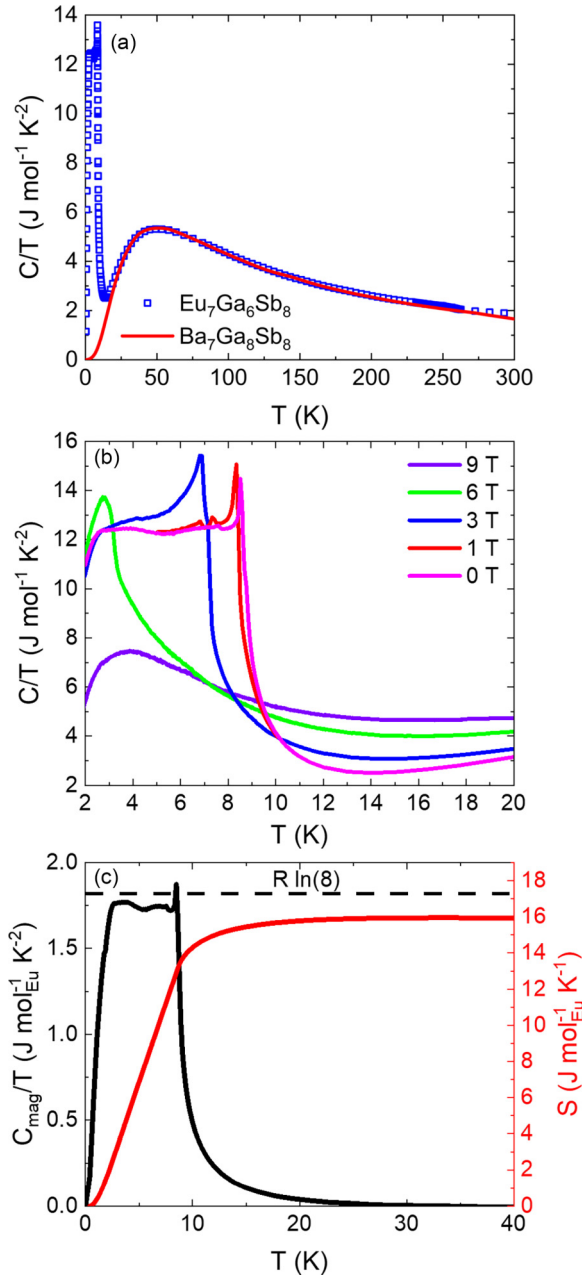


FIG. 4. (a) Specific heat over temperature of  $\text{Eu}_7\text{Ga}_6\text{Sb}_8$ . The red line represents  $C/T$  of the nonmagnetic analog  $\text{Ba}_7\text{Ga}_8\text{Sb}_8$ , which was used to subtract the lattice contribution. Inset: Anomaly in the high-temperature specific heat from a structural phase transition. (b) Magnetic field dependence of  $C(T)/T$ . The sharp transition is due to AFM order. (c) Left axis: Magnetic specific heat divided by temperature versus temperature. Right axis: Magnetic entropy versus temperature from the integration of the magnetic specific heat. The dashed line corresponds to the entropy expected for divalent Eu system with  $S = 7/2$ .

Figure 5(b) is a plot of the temperature dependence of the thermal expansion coefficient  $\alpha$  at various magnetic fields. The extrema of peaks in the derivative of  $\alpha(T)$  are plotted on the magnetic phase diagram in Fig. 6, as well as points taken from  $\chi(T)$  and  $C(T)/T$ . The AFM phase boundary is consistent across these three experiments.

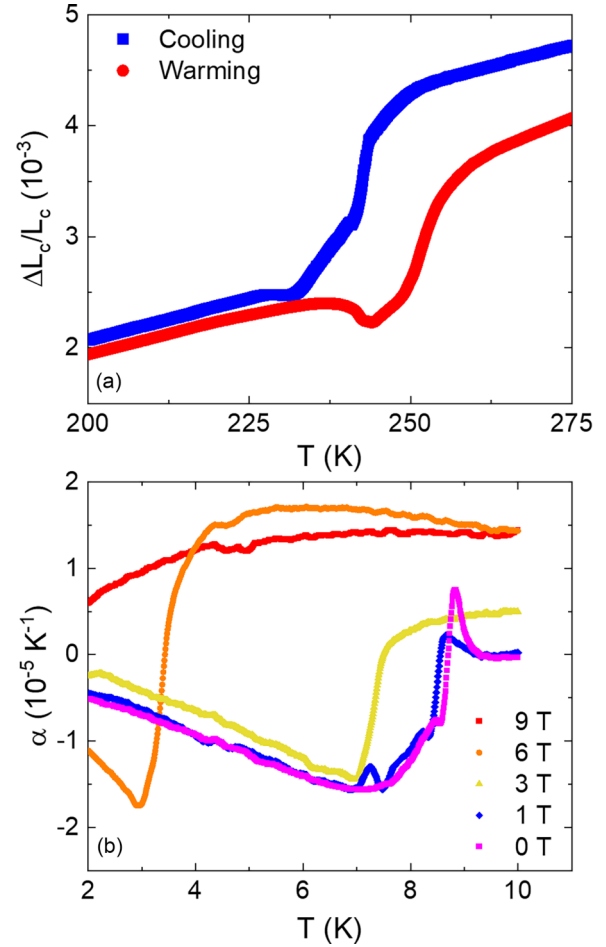


FIG. 5. (a) Anomaly in the high-temperature  $\Delta L_c/L_c$  upon initial cool-down and warm-up of sample which signals a structural phase transition. (b) Anomalies in the thermal expansion coefficient  $\alpha$  at various magnetic field values due to an AFM phase transition.

## F. Theoretical calculations

DFT electronic structure calculations of the band structure and density of states, shown in Figs. 7(a) and 7(b), respectively, were performed using the experimental low-temperature  $Pbca$  crystal structure, shown in Fig. 7(c), as well as a geometrically optimized crystal structure. The relaxed lattice parameters were  $a = 15.689 \text{ \AA}$ ,  $b = 17.267 \text{ \AA}$ , and  $c = 17.969 \text{ \AA}$ , in good agreement with the experimental lattice parameters  $a = 15.647 \text{ \AA}$ ,  $b = 17.288 \text{ \AA}$ , and  $c = 17.920 \text{ \AA}$  [1]. Structural relaxation caused only a small reduction in the band gap relative to the experimental crystal structure, from 0.47 eV to 0.40 eV, and did not qualitatively change the band structure. The element-projected density of states indicates that the valence band and conduction band are highly hybridized between Eu, Ga, and Sb, with a slight dominance by Eu and Sb in the valence band and conduction band, respectively.

To determine the sensitivity of the band gap to the presence of  $f$  electrons, the band structures were first calculated in a nonmagnetic state with the Eu  $f$  electrons localized within the core. As shown in Fig. 7(d), the spin-polarized band structure was calculated while explicitly including the Eu  $f$  electrons

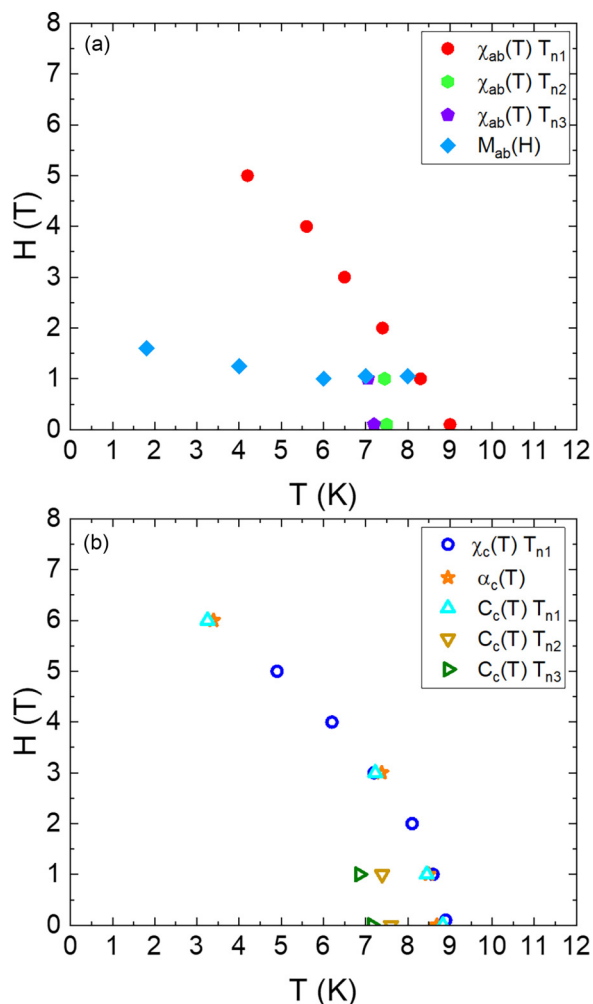


FIG. 6.  $H$ - $T$  phase diagram that has been determined for (a)  $H \perp c$  and (b)  $H \parallel c$ .

with a Hubbard- $U$  correction as suggested and implemented by Dudarev *et al.* [43] to account for the localized nature of  $f$  electrons using  $U = 6.0$  eV for Eu. As a first approximation to the actual magnetic structure, collinear antiferromagnetic ordering was applied to the Eu  $f$  electrons with alternating layers of Eu ions in the  $ac$  plane adopting alternating spin states. Incorporation of the  $f$  electrons into the band structure calculation decreased the band gap slightly to 0.31 eV. The calculated magnetic moments were  $6.98 \mu_B$  per Eu ion. The GGA+ $U$  band structure was very similar to the GGA band structure near the band gap, with the localized  $f$  electron bands appearing  $-1.5$  eV below the valence band maximum. As increasing the Hubbard- $U$  value to more accurately capture the larger experimentally measured magnetic moment per Eu ion would be expected to shift the Eu  $f$  bands further from the Fermi energy, it is reasonable to assume the Eu  $f$  electrons do not substantially affect the band gap. It should be noted that while spin-orbit coupling (SOC) is expected to be relevant due to the large atomic number of Eu, the 168 atoms in the unit cell rendered calculations including SOC intractable. As SOC would not be expected to substantially change the qualitative electronic structure, such as by closing the band gap entirely, the conclusions drawn from the calculations without SOC

remain valid. These calculations indicate that the intrinsic ground state of  $\text{Eu}_7\text{Ga}_6\text{Sb}_8$  is a charge-balanced insulator with a direct band gap of  $\Delta \approx 0.4$  eV.

#### IV. DISCUSSION AND SUMMARY

The structure of  $\text{Eu}_7\text{Ga}_6\text{Sb}_8$  features 2D layers of Eu ions arranged in a distorted triangular lattice. These layers are separated by anionic chains of hexagonally close packed  $[\text{Ga}_6\text{Sb}_8]^{14-}$  units with Eu ions occupying the interstitial spaces [1]. A structural phase transition is observed at approximately 250 K, with signatures present in resistivity, specific heat, and thermal expansion. High-resolution PXRD data also confirm this transition. Pawley refinements of the data at room temperature suggest the structure to crystallize in space group  $Cmcm$ . At 180 K, Rietveld refinements of the data were indicative of the space group  $Pbca$ , which has a lower symmetry. This is not surprising when considering the layered structure of this material, where the details of interlayer bonding states can be crucial to the resulting crystalline symmetry [15].

The magnetism in  $\text{Eu}_7\text{Ga}_6\text{Sb}_8$  shows complex behavior that is a result of the orthorhombic symmetry of the lattice as well as a disordered structure with 7 unique  $\text{Eu}^{2+}$  sites. Both specific heat and magnetization measurements are indicative of long-range AFM ordering of  $\text{Eu}^{2+}$  moments ( $S = 7/2$ ) at  $T_{n1} = 9.0$  K, with two spin-reorientation transitions at  $T_{n2} = 7.5$  K and  $T_{n3} = 7.2$  K. The positive high-temperature Weiss temperature is in contrast with the AFM phase at low temperatures, suggesting a competition of FM and AFM interactions. Magnetic anisotropy is observed in the low-temperature  $\chi(T)$  and  $M(H)$  data and is expected from the complex exchange interactions. The analysis of  $\chi(T)$  and  $M(H)$  reveals that the AFM easy axis lies within the  $ab$  plane and that the magnetic structure is likely coplanar.

DFT calculations that were performed under several different assumptions all show a direct band gap of approximately 0.4 eV at the  $\Gamma$  point. This is in contrast with electrical resistivity data that show a weak metallic behavior in the range  $25 \text{ K} < T < 200 \text{ K}$ . There are many instances in which semiconductors have been observed to have metallic conduction [60–62]. This is usually attributed to doping and disorder, where an impurity band forms within the gap. Disorder in the form of vacancies or antisite defects has been shown to be the origin of metallic conduction in GeTe, which is predicted to be a semiconductor with a band gap of at least 0.4 eV [63]. In the case of  $\text{Eu}_7\text{Ga}_6\text{Sb}_8$ , previous work as well as this report have found that the crystals form with excess Sb as well as a deficient amount of Ga. These defect sites likely contribute to the thermodynamic stability of the room-temperature phase, as EDX measurements are consistent across multiple experiments. This is also the likely origin of the observed metallic conduction in this compound. The rise in electrical resistivity below 20 K can be explained under the same picture, as impurity carriers in a lightly doped semiconductor can be frozen out at low temperatures. This can result in nonactivated behavior, as these trapped carriers can be re-excited with sufficient electric field [64].

A final consideration is that there may be multiple parallel conduction channels within the single crystals which appear as the sample is brought through the structural phase

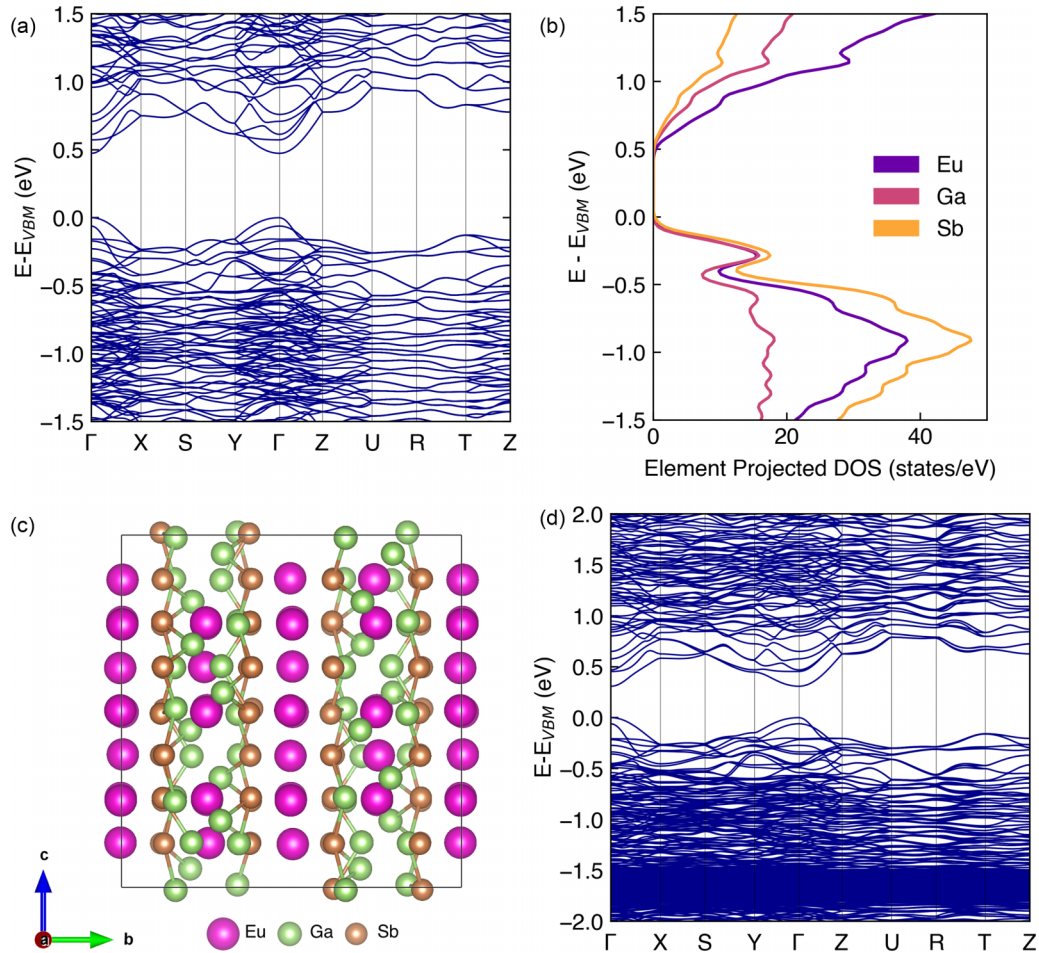


FIG. 7. (a) Electronic band structure and (b) element projected density of states of  $\text{Eu}_7\text{Ga}_6\text{Sb}_8$  using the experimentally determined lattice parameters. (c) Unit cell of the crystal structure of  $\text{Eu}_7\text{Ga}_6\text{Sb}_8$  containing 168 ions, with Eu in magenta, Ga in green, and Sb in bronze. (d) Electronic band structure of  $\text{Eu}_7\text{Ga}_6\text{Sb}_8$  including Eu  $f$  electrons with a Hubbard- $U$  correction, where  $U = 6.0$  eV. The zero of the energy axis for plots (a), (b), and (d) have been shifted to the valence band maximum.

transition. As stated earlier, temperature cycling of this compound usually results in cracks forming, with the sample eventually breaking into many pieces after several cycles. This will result in a masking of the intrinsic conduction mechanism at low temperatures.

Our work highlights the role of disorder in electrical transport properties of complex structures that adhere to the Zintl concept and the possible disconnect between DFT predictions and experimental results. Here we postulate that disorder in  $\text{Eu}_7\text{Ga}_6\text{Sb}_8$  is caused by several different parameters. First, off-stoichiometry of this material contributes to impurity band conduction, which manifests in weak metallic resistivity over a large temperature range. Second, irreversible structural damage occurs when cycling temperature from room temperature to liquid-helium temperatures. This damage likely occurs as cracks in the crystal through the structural phase transition where the crystal structure goes from a higher-symmetry space group to a more disordered and lower-symmetry arrangement. These features result in electrical transport that does not follow the expected semiconducting behavior from DFT calculations. Future work could lead to further exploration of disordered Zintl phase compounds for their thermoelectric properties, as one would expect a low thermal

conductivity intrinsic to this type of complex structure which may be paired with good electrical conductivity from in-gap states.

#### ACKNOWLEDGMENTS

Work at Los Alamos National Laboratory was performed under the auspices of the U.S. Department of Energy, Office of Basic Energy Sciences, Division of Materials Science and Engineering. Scanning electron microscope and energy-dispersive x-ray measurements were performed at the Center for Integrated Nanotechnologies, an Office of Science User Facility operated for the U.S. Department of Energy Office of Science. Computational resources were supported by the Center for Integrated Nanotechnologies, a DOE Office of Science user facility, in partnership with the LANL Institutional Computing Program for computational resources. Additional computations were performed at the National Energy Research Scientific Computing Center (NERSC), a U.S. Department of Energy Office of Science user facility located at Lawrence Berkeley National Laboratory, operated under Contract No. DE-AC02-05CH11231 using NERSC Award No. ERCAP0020494. This research used resources of the



Advanced Photon Source, a U.S. Department of Energy (DOE) Office of Science user facility operated for the DOE Office of Science by Argonne National Laboratory under

Contract No. DE-AC02-06CH11357. M.S.C. acknowledges support from the Laboratory Directed Research and Development program.

- [1] S.-M. Park, S.-J. Kim, and M. G. Kanatzidis, Eu<sub>7</sub>Ga<sub>6</sub>Sb<sub>8</sub>: A Zintl phase with Ga-Ga bonds and polymeric gallium antimonide chains, *J. Solid State Chem.* **177**, 2867 (2004).
- [2] S. M. Kauzlarich, Special issue: Advances in Zintl phases, *Materials* **12**, 2554 (2019).
- [3] A. Ovchinnikov and S. Bobev, Zintl phases with group 15 elements and the transition metals: A brief overview of pnictides with diverse and complex structures, *J. Solid State Chem.* **270**, 346 (2019).
- [4] H. Luo, J. W. Krizan, L. Muechler, N. Haldolaarachchige, T. Klimczuk, W. Xie, M. K. Fuccillo, C. Felser, and R. J. Cava, A large family of filled skutterudites stabilized by electron count, *Nat. Commun.* **6**, 6489 (2015).
- [5] S. Bobev, J. D. Thompson, J. L. Sarrao, M. M. Olmstead, H. Hope, and S. M. Kauzlarich, Probing the limits of the Zintl concept: Structure and bonding in rare-earth and alkaline-earth zinc-antimonides Yb<sub>9</sub>Zn<sub>4+x</sub>Sb<sub>9</sub> and Ca<sub>9</sub>Zn<sub>4.5</sub>Sb<sub>9</sub>, *Inorg. Chem.* **43**, 5044 (2004).
- [6] R. Lam and A. Mar, The metallic Zintl phase Ba<sub>3</sub>Sn<sub>4</sub>As<sub>6</sub>, *Solid State Sci.* **3**, 503 (2001).
- [7] U. Aydemir, A. Ormeci, H. Borrmann, B. Böhme, F. Zürcher, B. Uslu, T. Goebel, W. Schnelle, P. Simon, W. Carrillo-Cabrera, F. Haarmann, M. Baitinger, R. Nesper, H. G. von Schnering, and Y. Grin, The metallic Zintl phase Ba<sub>3</sub>Si<sub>4</sub>: Synthesis, crystal structure, chemical bonding, and physical properties, *Z. Anorg. Allg. Chem.* **634**, 1651 (2008).
- [8] A. Ker, E. Todorov, R. Rousseau, K. Uehara, F.-X. Lannuzel, and J. S. Tse, Structure and phase stability of binary Zintl-phase compounds: Lithium—group 13 intermetallics and metal-doped group 14 clathrate compounds, *Chem. Eur. J.* **8**, 2787 (2002).
- [9] A. R. Eulenstein, D. Bogdanovski, H. Reinhardt, V. Miß, B. Røling, N. Hampf, R. Dronskowski, and S. Dehnen, K<sub>2</sub>Ge<sub>3</sub>As<sub>3</sub>: Fiberlike crystals of a narrow-band-gap Zintl phase with a one-dimensional substructure  $\infty^1\{(\text{Ge}_3\text{As}_3)^{2-}\}$ , *Chem. Mater.* **31**, 8839 (2019).
- [10] H. Ehrenberg, H. Pauly, T. Hansen, J.-C. Jaud, and H. Fuess, Phase transition from the cubic Zintl phase LiIn into a tetragonal structure at low temperature, *J. Solid State Chem.* **167**, 1 (2002).
- [11] W.-T. Guo, Z. Huang, and J.-M. Zhang, The Zintl phase compounds AEIn<sub>2</sub>As<sub>2</sub> (AE = Ca, Sr, Ba): Topological phase transition under pressure, *Phys. Chem. Chem. Phys.* **24**, 17337 (2022).
- [12] R. Umamaheswari, M. Yogeswari, and G. Kalpana, Electronic properties and structural phase transition in A<sub>4</sub> [M<sub>4</sub>O<sub>4</sub>] (A=Li, Na, K and Rb; M=Ag and Cu): A first principles study, *Solid State Commun.* **155**, 62 (2013).
- [13] N. E. Christensen, Electronic structure and bonding in ternary Zintl phases: LiAlSi, *Phys. Rev. B* **32**, 6490 (1985).
- [14] C. Li, F. Ke, Q. Hu, Z. Yu, J. Zhao, Z. Chen, and H. Yan, Correlated structural and electronic phase transformations in transition metal chalcogenide under high pressure, *J. Appl. Phys.* **119**, 135901 (2016).
- [15] H.-J. Kim, S.-H. Kang, I. Hamada, and Y.-W. Son, Origins of the structural phase transitions in MoTe<sub>2</sub> and WTe<sub>2</sub>, *Phys. Rev. B* **95**, 180101(R) (2017).
- [16] Y. Xiao, M. Zhou, J. Liu, J. Xu, and L. Fu, Phase engineering of two-dimensional transition metal dichalcogenides, *Sci. China Mater.* **62**, 759 (2019).
- [17] H. Yang, S. W. Kim, M. Chhowalla, and Y. H. Lee, Structural and quantum-state phase transitions in van der Waals layered materials, *Nat. Phys.* **13**, 931 (2017).
- [18] N. C. Gresty, Y. Takabayashi, A. Y. Ganin, M. T. McDonald, J. B. Claridge, D. Giap, Y. Mizuguchi, Y. Takano, T. Kagayama, Y. Ohishi, M. Takata, M. J. Rosseinsky, S. Margadonna, and K. Prassides, Structural phase transitions and superconductivity in Fe<sub>1+δ</sub>Se<sub>0.57</sub>Te<sub>0.43</sub> at ambient and elevated pressures, *J. Am. Chem. Soc.* **131**, 16944 (2009).
- [19] S. M. Kauzlarich, S. R. Brown, and G. Jeffrey Snyder, Zintl phases for thermoelectric devices, *Dalton Trans.* **2007**, 2099 (2007).
- [20] Z. M. Elqahtani, S. Aman, S. Mehmood, Z. Ali, A. Hussanan, N. Ahmad, S. Alomairy, M. S. Al-Buriahi, Z. A. Alrowaili, and H. M. T. Farid, *n*-Type narrow band gap A<sub>3</sub>InAs<sub>3</sub> (A = Sr and Eu) Zintl phase semiconductors for optoelectronic and thermoelectric applications, *J. Taibah University Sci.* **16**, 660 (2022).
- [21] T. Seddik, G. Uğur, R. Khenata, Ş. Uğur, F. Soyalp, G. Murtaza, D. P. Rai, A. Bouhemadou, and S. Bin Omran, Optoelectronic and thermoelectric properties of Zintl YLi<sub>3</sub>A<sub>2</sub> (A = Sb, Bi) compounds through modified Becke-Johnson potential, *Chinese Phys. B* **25**, 107801 (2016).
- [22] J. A. Brehm, Predicted bulk photovoltaic effect in hydrogenated Zintl compounds, *J. Mater. Chem. C* **6**, 1470 (2018).
- [23] A. Werwein, C. Benndorf, M. Bertmer, A. Franz, O. Oeckler, and H. Kohlmann, Hydrogenation properties of LnAl<sub>2</sub> (Ln = La, Eu, Yb), LaGa<sub>2</sub>, LaSi<sub>2</sub> and the crystal structure of LaGa<sub>2</sub>H<sub>0.71(2)</sub>, *Crystals* **9**, 193 (2019).
- [24] K. L. Hodge and J. E. Goldberger, Transition metal-free alkyne hydrogenation catalysis with BaGa<sub>2</sub>, a hydrogen absorbing layered Zintl phase, *J. Am. Chem. Soc.* **141**, 19969 (2019).
- [25] P. Rosa, Y. Xu, M. Rahn, J. Souza, S. Kushwaha, L. Veiga, A. Bombardi, S. Thomas, M. Janoschek, E. Bauer, M. Chan, Z. Wang, J. Thompson, N. Harrison, P. Pagliuso, A. Bernevig, and F. Ronning, Colossal magnetoresistance in a nonsymmorphic antiferromagnetic insulator, *npj Quantum Mater.* **5**, 52 (2020).
- [26] L.-L. Wang, A. Kaminski, P. C. Canfield, and D. D. Johnson, Different topological quantum states in ternary Zintl compounds: BaCaX (X = Si, Ge, Sn and Pb), *J. Phys. Chem. C* **122**, 705 (2018).
- [27] M. O. Ogunbunmi, S. Baranets, A. B. Childs, and S. Bobev, The Zintl phases AIn<sub>2</sub>As<sub>2</sub> (A = Ca, Sr, Ba): New topological insulators and thermoelectric material candidates, *Dalton Trans.* **50**, 9173 (2021).

- [28] T. Zhang, C. Yue, T. Zhang, S. Nie, Z. Wang, C. Fang, H. Weng, and Z. Fang, Topological crystalline insulators with  $C_2$  rotation anomaly, *Phys. Rev. Res.* **1**, 012001(R) (2019).
- [29] Z. Zhu, M. Li, and J. Li, Topological semimetal to insulator quantum phase transition in the Zintl compounds  $Ba_2X$  ( $X = Si, Ge$ ), *Phys. Rev. B* **94**, 155121 (2016).
- [30] J. Wang, X. Cui, Y. Wan, T. Ying, S. Li, and J. Guo, Superconductivity in layered Zintl phase  $LiSn_2As_2$ , [arXiv:2111.11319](https://arxiv.org/abs/2111.11319).
- [31] L. Deakin, R. Lam, F. Marsiglio, and A. Mar, Superconductivity in  $Ba_2Sn_3Sb_6$  and  $SrSn_3Sb_4$ , *J. Alloys Compd.* **338**, 69 (2002).
- [32] B. C. Sales, R. Jin, and D. Mandrus, Zintl compounds: From power generation to the anomalous Hall effect, *J. Phys. Soc. Jpn.* **77**, 48 (2008).
- [33] A. M. Goforth, P. Klavins, J. C. Fettinger, and S. M. Kauzlarich, Magnetic properties and negative colossal magnetoresistance of the rare earth Zintl phase  $EuIn_2As_2$ , *Inorg. Chem.* **47**, 11048 (2008).
- [34] S. Sarkar, M. J. Gutmann, and S. C. Peter, The crystal structure and magnetic properties of a Zintl phase  $EuIrIn_4$ : The first member of the Eu-Ir-In family, *Dalton Trans.* **43**, 15879 (2014).
- [35] J. Jiang, A. C. Payne, M. M. Olmstead, H.-o. Lee, P. Klavins, Z. Fisk, S. M. Kauzlarich, R. P. Hermann, F. Grandjean, and G. J. Long, Complex magnetic ordering in  $Eu_3InP_3$ : A new rare earth metal Zintl compound, *Inorg. Chem.* **44**, 2189 (2005).
- [36] J. Jiang and S. M. Kauzlarich, Colossal magnetoresistance in a rare earth Zintl compound with a new structure type:  $EuIn_2P_2$ , *Chem. Mater.* **18**, 435 (2006).
- [37] T. Degen, M. Sadki, E. Bron, U. König, and G. Néner, The HighScore suite, *Powder Diffr.* **29**, S13 (2014).
- [38] G. M. Schmiedeshoff, A. W. Lounsbury, D. J. Luna, S. J. Tracy, A. J. Schramm, S. W. Tozer, V. F. Correa, S. T. Hannahs, T. P. Murphy, E. C. Palm, A. H. Lacerda, S. L. Bud'ko, P. C. Canfield, J. L. Smith, J. C. Lashley, and J. C. Cooley, Versatile and compact capacitive dilatometer, *Rev. Sci. Instrum.* **77**, 123907 (2006).
- [39] G. Kresse and D. Joubert, From ultrasoft pseudopotentials to the projector augmented-wave method, *Phys. Rev. B* **59**, 1758 (1999).
- [40] G. Kresse and J. Furthmüller, Efficiency of *ab-initio* total energy calculations for metals and semiconductors using a plane-wave basis set, *Comput. Mater. Sci.* **6**, 15 (1996).
- [41] G. Kresse and J. Furthmüller, Efficient iterative schemes for *ab initio* total-energy calculations using a plane-wave basis set, *Phys. Rev. B* **54**, 11169 (1996).
- [42] J. P. Perdew, K. Burke, and M. Ernzerhof, Generalized Gradient Approximation Made Simple, *Phys. Rev. Lett.* **77**, 3865 (1996).
- [43] S. L. Dudarev, G. A. Botton, S. Y. Savrasov, C. J. Humphreys, and A. P. Sutton, Electron-energy-loss spectra and the structural stability of nickel oxide: An LSDA+U study, *Phys. Rev. B* **57**, 1505 (1998).
- [44] G. S. Pawley, Unit-cell refinement from powder diffraction scans, *J. Appl. Crystallogr.* **14**, 357 (1981).
- [45] J. Y. Chan, M. E. Wang, A. Rehr, S. M. Kauzlarich, and D. J. Webb, Synthesis, structure, and magnetic properties of the rare-earth Zintl compounds  $Eu_{14}MnPn_{11}$  and  $Eu_{14}InPn_{11}$  ( $Pn = Sb, Bi$ ), *Chem. Mater.* **9**, 2131 (1997).
- [46] M. Marshall, I. Pletikosić, M. Yahyavi, H.-J. Tien, T.-R. Chang, H. Cao, and W. Xie, Magnetic and electronic structures of antiferromagnetic topological material candidate  $EuMg_2Bi_2$ , *J. Appl. Phys.* **129**, 035106 (2021).
- [47] V. K. Anand and D. C. Johnston, Metallic behavior induced by potassium doping of the trigonal antiferromagnetic insulator  $EuMn_2As_2$ , *Phys. Rev. B* **94**, 014431 (2016).
- [48] J. Blawat, M. Marshall, J. Singleton, E. Feng, H. Cao, W. Xie, and R. Jin, Unusual electrical and magnetic properties in layered  $EuZn_2As_2$ , *Adv. Quantum Tech.* **5**, 2200012 (2022).
- [49] J.-Z. Ma, S. M. Nie, C. J. Yi, J. Jandke, T. Shang, M. Y. Yao, M. Naamneh, L. Q. Yan, Y. Sun, A. Chikina, V. N. Strocov, M. Medarde, M. Song, Y.-M. Xiong, G. Xu, W. Wulfhökel, J. Mesot, M. Reticioli, C. Franchini, C. Mudry *et al.*, Spin fluctuation induced Weyl semimetal state in the paramagnetic phase of  $EuCd_2As_2$ , *Sci. Adv.* **5**, eaaw4718 (2019).
- [50] T. Berry, V. J. Stewart, B. W. Y. Redemann, C. Lygouras, N. Varnava, D. Vanderbilt, and T. M. McQueen, A-type antiferromagnetic order in the Zintl phase insulator  $EuZn_2P_2$ , *Phys. Rev. B* **106**, 054420 (2022).
- [51] P. Rosa, C. de Jesus, Z. Fisk, and P. Pagliuso, Physical properties of  $EuPtIn_4$  intermetallic antiferromagnet, *J. Magn. Magn. Mater.* **371**, 5 (2014).
- [52] S. Pakhira, F. Islam, E. O'Leary, M. A. Tanatar, T. Heitmann, L.-L. Wang, R. Prozorov, A. Kaminski, D. Vaknin, and D. C. Johnston, A-type antiferromagnetic order in semiconducting  $EuMg_2Sb_2$  single crystals, *Phys. Rev. B* **106**, 024418 (2022).
- [53] T. Berry, S. R. Parkin, and T. M. McQueen, Antiferro- and metamagnetism in the  $S = 7/2$  hollandite analog  $EuGa_2Sb_2$ , *Phys. Rev. Mater.* **5**, 114401 (2021).
- [54] K. G. Raj and P. A. Joy, Cross over from 3D variable range hopping to the 2D weak localization conduction mechanism in disordered carbon with the extent of graphitization, *Phys. Chem. Chem. Phys.* **17**, 16178 (2015).
- [55] B. I. Shklovskii and A. L. Efros, Variable-range hopping conduction, in *Electronic Properties of Doped Semiconductors*, edited by M. Cardona, P. Fulde, and H.-J. Queisser (Springer, Berlin, 1984), pp. 202–227.
- [56] T. C. Harman, H. L. Goering, and A. C. Beer, Electrical properties of *n*-type InAs, *Phys. Rev.* **104**, 1562 (1956).
- [57] R. Radwanski, D. Nalecz, S. Fedyk, and Z. Ropka,  $EuTiO_3$ : The low-energy electronic structure of  $Eu^{2+}$  from the specific heat, *Mater. Chem. Phys.* **186**, 426 (2017).
- [58] Y. Misawa, Y. Doi, and Y. Hinatsu, Magnetic ordering of divalent europium in double perovskites  $Eu_2LnTaO_6$  ( $Ln =$  rare earths), *J. Solid State Chem.* **184**, 1478 (2011).
- [59] J. A. Quilliam, K. A. Ross, A. G. Del Maestro, M. J. P. Gingras, L. R. Corruccini, and J. B. Kycia, Evidence for Gapped Spin-Wave Excitations in the Frustrated  $Gd_2Sn_2O_7$  Pyrochlore Antiferromagnet from Low-Temperature Specific Heat Measurements, *Phys. Rev. Lett.* **99**, 097201 (2007).
- [60] S. I. Kim, S. Hwang, S. Y. Kim, W.-J. Lee, D. W. Jung, K.-S. Moon, H. J. Park, Y.-J. Cho, Y.-H. Cho, J.-H. Kim, D.-J. Yun, K. H. Lee, I.-t. Han, K. Lee, and Y. Sohn, Metallic conduction induced by direct anion site doping in layered  $SnSe_2$ , *Sci. Rep.* **6**, 19733 (2016).
- [61] A. Jaoui, G. Seyfarth, C. W. Rischau, S. Wiedmann, S. Benhabib, C. Proust, K. Behnia, and B. Fauqué, Giant Seebeck

- effect across the field-induced metal-insulator transition of InAs, [npj Quantum Mater.](#) **5**, 94 (2020).
- [62] M. Benzaquen, D. Walsh, and K. Mazuruk, Conductivity of *n*-type GaAs near the Mott transition, [Phys. Rev. B](#) **36**, 4748 (1987).
- [63] A. H. Edwards, A. C. Pineda, P. A. Schultz, M. G. Martin, A. P. Thompson, and H. P. Hjalmarson, Theory of persistent, *p*-type, metallic conduction in c-GeTe, [J. Phys.: Condens. Matter](#) **17**, L329 (2005).
- [64] Z. Q. Liu, D. P. Leusink, X. Wang, W. M. Lu, K. Gopinadhan, A. Annadi, Y. L. Zhao, X. H. Huang, S. W. Zeng, Z. Huang, A. Srivastava, S. Dhar, T. Venkatesan, and Ariando, Metal-Insulator Transition in SrTiO<sub>3-x</sub> Thin Films Induced by Frozen-Out Carriers, [Phys. Rev. Lett.](#) **107**, 146802 (2011).